RESEARCH ARTICLE

PLASMA PROCESSES AND POLYMERS

Coarse-grained approach to amorphous and anisotropic materials in kinetic Monte Carlo thin-film growth simulations: A case study of TiO$_2$ and ZnO by plasma-enhanced chemical vapor deposition

Jorge Budagosky | Xabier García-Casas | Juan R. Sánchez-Valencia |
Ángel Barranco | Ana Borrás

Nanotechnology on Surfaces and Plasma Group, Materials Science Institute of Seville (CSIC-US), Seville, Spain

Correspondence
Jorge Budagosky and Ana Borrás, Nanotechnology on Surfaces and Plasma Group, Materials Science Institute of Seville (CSIC-US), C/Américo Vespucio 49, Seville 41092, Spain.
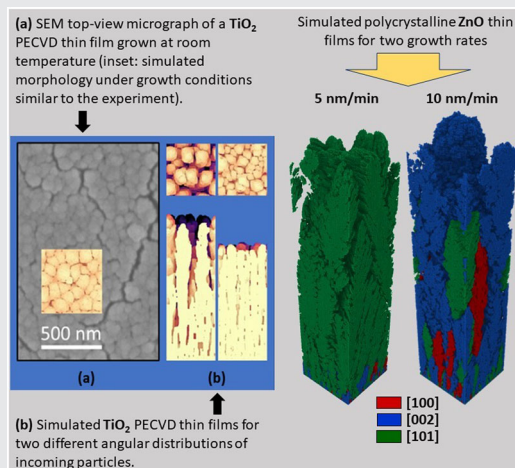Email: jorge.budagosky@icmse.csic.es and anaisabel.borras@icmse.csic.es

Abstract

The growth of TiO$_2$ and ZnO thin films is studied by means of coarse-grained kinetic Monte Carlo simulations under conditions typically encountered in plasma-enhanced chemical vapor deposition experiments. The basis of our approach is known to work well to simulate the growth of amorphous materials using cubic grids and is extended here to reproduce not only the morphological characteristics and scaling properties of amorphous TiO$_2$ but also the growth of polycrystalline ZnO with a good approximation, including the evolution of the film texture during growth and its dependence on experimental conditions. The results of the simulations have been compared with available experimental data obtained by X-ray diffraction, analysis of the texture coefficients, atomic force microscopy, and scanning electron microscopy.

(a) SEM top-view micrograph of a **TiO$_2$** PECVD thin film grown at room temperature (inset: simulated morphology under growth conditions similar to the experiment).

(b) Simulated **TiO$_2$** PECVD thin films for two different angular distributions of incoming particles.

Simulated polycrystalline **ZnO** thin films for two growth rates

5 nm/min   10 nm/min

[100] [002] [101]

KEYWORDS
amorphous, anisotropy, kinetic Monte Carlo (KMC), plasma-enhanced chemical vapor deposition (PE-CVD), polycrystalline, texturization, TiO$_2$, ZnO

Abbreviations: BKL, Bortz–Kalos–Lebowitz; CG, coarse-grained; ECR, Electron-cyclotron Resonance; KMC, kinetic Monte Carlo; MD, molecular dynamics; PECVD, plasma-enhanced chemical vapor deposition; RMS, root mean square; RT, room temperature; SEM, scanning electron microscopy; XRD, X-ray diffraction.

1 | INTRODUCTION

Growth simulations tools are extremely important to reveal the mechanisms responsible for the structural features in thin films and low dimensional materials and the relationships with their physicochemical and functional properties. Thus, there is an ever-increasing interest in the development of simulation models with adaptability and flexibility to encompass predictive analysis on the deposition of simple and hetero-structured materials. The major aim is to provide straightforward paths in the experimental routes toward the optimization of the properties and final performance in the targeted applications. Depending on the scale and nature of the features to be studied, the simulations usually range from those based on molecular dynamics (MD),[1,2] kinetic Monte Carlo (KMC),[3,4] or hybrid methods[5–8] to continuum methods.[9–12] There is a wide range of technological applications for which the growth of thin films in multilayer systems (or even in more complex nanostructures) is a fundamental part. In many cases, the systems studied cover scales that are too large to be efficiently simulated by microscopic methods (e.g., MD and atomistic KMC), while at the same time show morphological characteristics that are difficult to simulate using continuous methods. It is in this *no-man's-land* where a coarse-grained (CG) treatment of the KMC method is often useful.[13–24]

From a technological point of view, TiO_2 is part of a set of materials of intensive use in the manufacture of optoelectronic nano-devices, antireflective coatings, and antibacterial, biocompatible, antifogging, and self-cleanable surfaces. The control of the microstructure of the thin layers of this material is therefore an aspect that has been extensively studied before. Several simple models have been used previously to explain the anomalous roughness scaling behavior observed under various growth techniques.[14–17,19,20,22] Since the growth methods usually employed in the manufacture of amorphous thin films tend to operate in the low-temperature range and involve highly reactive surfaces, most of the models used to simulate the morphology of amorphous materials (e.g., TiO_2, SiO_2, Nb_2O_5, etc.) resort to various approaches that greatly restrict the range of growing conditions in which they can be applied. In this study, we have developed a KMC-based model that considers many of the general characteristics of those models but includes fewer constraints. This permits it to cover a wider range of growing conditions, thus allowing its straightforward application to other materials. However, concerning the results shown here, these have focused on simulating growth processes under typical conditions found in the plasma-enhanced chemical vapor deposition (PECVD) technique. Such a deposition method has been applied during the last two decades in the development of functional coatings with applications in areas ranging from optics to biomaterials, including microelectronics and energy. During the last years, PECVD has been also extended to the fabrication of nanoscale materials, as nanoporous thin films and low dimensional nanostructures beyond graphene, CNTs and nanowalls[25-28] like, for instance, metal oxide nanorods and core@shell nanowires and nanotubes in combination with hard and soft template methods.[29–32]

Thus, looking for the demonstration of the universal character of the proposed model, we have also approached the description of the crystalline anisotropic growth. Concretely, we have made emphasis in the simulation of the one-dimensional formation commonly observed in ZnO thin films grown by PECVD.[31,33] The model is capable of reproducing, with a good approximation, the formation of polycrystalline layers of anisotropic materials, retaining the simplicity associated with the use of a cubic grid in the simulations. Also, we can tune the morphology and texture of the film throughout an anisotropy parameter that may be associated directly with microscopic surface phenomena and its dependence on the growth conditions. These results are of paramount interest in the application of PECVD methodology for the fabrication of polycrystalline layers in nanodevices, as third-generation solar cells, including Dye-Sensitized Solar Cells and Perovskite Solar Cells, photocatalytic electrodes, and in the development of piezoelectric and pyroelectric nanogenerators.[34–40] In such applications, the precise control of the crystal growth parameters (crystal size, orientation, and texturization) allows for the design of nanomaterials with enhanced transport, optical, piezoelectric, and strain properties.

The paper is organized as follows, firstly, we describe the experimental setup used for the deposition and the analysis of the films, secondly, the theoretical background and the numerical method used in our simulations are described in detail. In the third place, we show and discuss the obtained predictions in comparison with the experimental results, and finally, we summarize the conclusions of our work.

2 | EXPERIMENTAL SECTION

TiO_2 and ZnO thin films were fabricated by PECVD at room temperature (RT). Titanium tetraisopropoxide ($C_{12}H_{28}O_4Ti$) and diethyl-zinc ((CH_2CH_3)$_2$Zn) precursors were purchased from Merck and used as delivered. Concretely, Ti precursor was inserted in the chamber by

bubbling oxygen through a mass flow controller, meanwhile, the Zn precursor was inserted through a regulable valve. The base pressure of the chamber was lower than 10^{-5} and 10^{-4} mbar for the TiO_2 and ZnO, correspondently. The total pressure during the deposition was around 10^{-2} mbar in both cases achieved by supplying oxygen to the plasma reactor. The plasma was generated in a 2.45 GHz micro-wave Electron-Cyclotron Resonance (ECR) SLAN-II operating at 400 W for TiO_2 and 800 W for ZnO. Scanning electron microscopic (SEM) micrographs were acquired in a Hitachi S4800 working at 2 kV at working distances in the range of 2–4 mm.

Fused silica and Si(100) substrates were emplaced below the precursor shower-like diffuser at a fixed position (without rotating). Samples with different thicknesses were prepared during the same experiment by employing a shutter close to the substrates. The shutter was kept closed until homogeneous precursor pressure within the chamber was reached under plasma presence to ensure reproducibility of the growing conditions for all the thicknesses. The substrate to precursor diffuser distance was 6 cm and to the plasma glow discharge 12 cm.

Root mean square (RMS) roughness was characterized by atomic force microscopy in a Nanotech microscope in tapping mode. X-ray diffraction (XRD) patterns were recorded in Panalytical X'PERT PRO diffractometer model operating in the θ–2θ configuration (Bragg-Brentano) and using the Cu Kα (1.5418 Å) radiation as an excitation source. The texture coefficients $T(hkl)$ were calculated applying the following equation:

$$T(hkl) = \frac{I(hkl)/I_0(hkl)}{\frac{1}{n}\sum I(hkl)/\sum I_0(hkl)}, \qquad (1)$$

where $I(hkl)$ and $I_0(hkl)$ are the peak intensities associated with the (hkl) family plane obtained in Bragg-Brentano ($\Theta - 2\Theta$) configuration for the samples and the randomly oriented reference pattern respectively (in this particular case the JCPDS card No. 36–1451, for wurtzite) and n is the number of possible reflections.

3 | THEORETICAL MODEL

The proposed model for the growth simulations is implemented within an event-based KMC scheme, developed by Bortz–Kalos–Lebowitz (BKL).[41] The code used to generate the simulation results shown in this study was developed in our group and is available from the authors upon reasonable request. The general features of the model are described as follows:

empty site   film   substrate
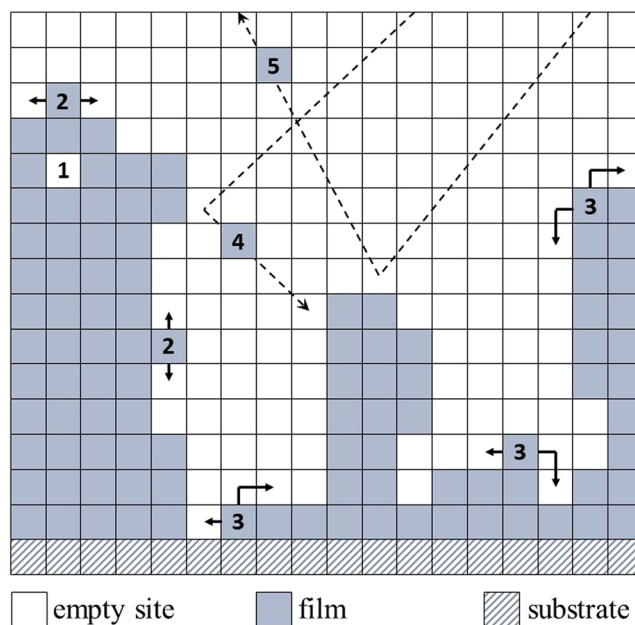
FIGURE 1 General scheme of the processes involved in the thin-film growth model developed in this study (for simplicity our 3D system is represented here in 2D). Several processes and configurations are included in the model: vacancies and overhangs are permitted (1; 2). A particle at the surface can jump randomly to any available site of six possible directions (2), except when a step is encountered (3), in that case, an extra jump is permitted. The deposition flux follows a distribution of trajectories for the incoming particles that may depend on the growth conditions. Once the particle reaches the surface, there is a possibility that it bounces and continues its journey with another trajectory until it reaches a new site (4) or until it reaches the roof of the simulation domain (5). If the latter occurs, that particle disappears and another particle is generated from scratch with a different trajectory and initial position at the roof

i) The system is defined by a simple 3D cubic lattice with a size $N_x \times N_y \times N_z$ and periodic boundary conditions along the directions of the growth plane (x, y). The 3D lattice is characterized by an integer array $G_{i,j,k}$ $(i = 1, ..., N_x; j = 1, ..., N_y; k = 1, ..., N_z)$ in which lateral overhangs and vacancies are allowed (see Figure 1). Here, $G_{i,j,k} = 0$ for empty sites, $G_{i,j,k} = 1$ for substrate particles, and $G_{i,j,k} > 1$ for particles of the film, with specific values that are related to the features of the model depending on whether one simulates an amorphous or an anisotropic material, as we will see later. In our model, the substrate particles are considered as immobile. In addition, although our model can simulate the growth of thin films on substrates with arbitrary morphology, we wanted to keep the simplicity of the initial conditions as much as possible for the proof-of-principles type results shown in this study.

Therefore, in all the cases considered here, the substrate is set as a single flat layer of particles, that is, $G_{i,j,k=1} = 1$ and $G_{i,j,k>1} = 0$. In concordance, the substrates applied in the fabrication consist of flat and low roughness surfaces, that is Si(100) and fused silica pieces. Each particle can perform a single site jump up to any available site in one of six possible directions associated with a cubic grid (left, right, back, front, up, down), except when a step is encountered in any direction of the 3D space. In that case, an extra jump to lower, upper, or lateral sites is possible within a single diffusion event (see particles with label 3 in Figure 1). The general constraint is that a particle must be bonded always to at least with one first neighbor.

To keep things simple, the size of all types of coarse particles is the same and equal to the step size of the 3D lattice, $\Delta x = \Delta y = \Delta z = a_0$. In the case of the anisotropic material, each deposited coarse particle individually contains all the information regarding its local crystallographic orientation with respect to the flat substrate. This feature will be elaborated on in more detail later. The size of the particles should be chosen as a compromise between computational performance and the pursued morphological detail.[18]

ii) The deposition of new particles onto the surface is performed at a rate of $r_0 = F \times N_X \times N_Y$, F being the net deposition flux (in monolayers per second, ML/s, with a monolayer being defined as a single full layer of particles). To simulate a flux of particles that mimics typical conditions encountered in PECVD, the following features are considered: the incoming particles are generated at an initial position in the 3D mesh that is defined as the roof of our simulation domain ($i_0, j_0, k_0 = N_{roof}$), where $N_{roof} \leq N_z$ while the coordinates i_0 and j_0 are picked randomly from a uniform distribution. The term N_{roof} is set as the maximum height of the surface profile plus one lattice unit; therefore, N_{roof} evolves with film thickness, while N_z is constant and is the maximum height of our simulation domain. This choice is justified since we are trying to simulate thin-film growth at low chamber pressure. Under these conditions, the mean free path of the incoming particles in the gas phase is very large compared with the surface features of the film and one can save computation time by avoiding the explicit simulation of the particle trip far above the surface since larger values of N_{roof} are statistically equivalent.[42]

The trajectory followed by the particle toward the surface is characterized by azimuthal φ_{dep} and polar θ_{dep} angles (Figure 2). These angles are obtained from an angular distribution that follows from a Maxwell-type distribution for the particle energies.[16] Within this model, the azimuthal angle is sampled from a uniform distribution $\varphi_{dep} \in [0,2\pi)$ while the polar angle is sampled via a distribution $g(\theta_{dep}, v_n)$ given by,

$$g(\theta_{dep}, v_n) = \frac{\int_0^{\theta_{dep}} F(\theta', v_n) d\theta'}{\int_0^{\pi/2} F(\theta', v_n) d\theta'}$$

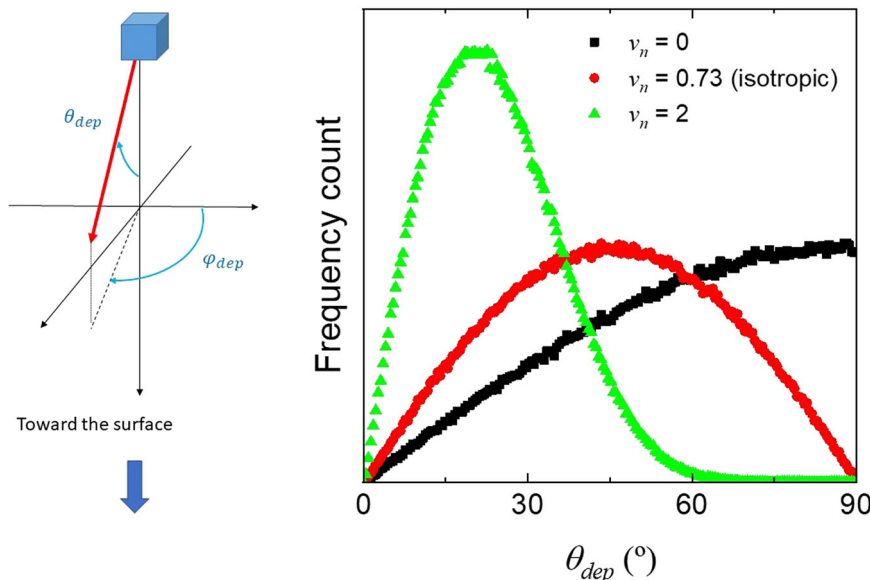$$= \int_0^{\theta_{dep}} F(\theta', v_n) d\theta', \qquad (2)$$

FIGURE 2 Angular distribution for the trajectories of the incoming particles toward the surface, considering three values of the normalized average velocity parameter v_n (see text for details)

where

$$F(\Theta, v_n) = 1$$
$$- \cos$$
$$\Theta \frac{\exp\left(v_n^2 \cos^2 \Theta\right)[1 + erf(v_n \cos \Theta)]}{\exp\left(v_n^2\right)[1 + erf(v_n)]} \quad (3)$$
$$.$$

The specific shape of the distribution is controlled through a normalized average velocity, v_n, directed toward the surface. Small values of v_n mean that the angular distribution function spreads the incoming direction of the particles. On the contrary, larger values correspond to a more collimated flux directed toward the surface, as can be seen in Figure 2. Once the set $(\theta_{dep}, \varphi_{dep})$ is obtained the trajectory of the particle during its fly is simulated by means of discrete jumps. Each jump is made up of simultaneous integer displacements $i_{dep} = \mathrm{Int}\left(\frac{r_{dep}}{\Delta x} \cos \varphi_{dep}\right)$, $j_{dep} = \mathrm{Int}\left(\frac{r_{dep}}{\Delta y} \sin \varphi_{dep}\right)$, and $k_{dep} = -1$ along directions x, y, and z, respectively, being $r_{dep} = \Delta z \tan \theta_{dep}$. This set of integers is calculated once at the beginning of the deposition event and the position of the flying particle (i, j, k) is changed accordingly at each displacement during the fly, that is $i \rightarrow i + i_{dep}, j \rightarrow j + j_{dep}, k \rightarrow k + k_{dep}$, looking around the particle after each movement to detect any possible neighbor in the new position. If more than one neighbor is detected in the new position the particle sticks there and it is considered attached to the film. On the contrary, if only one neighbor is encountered there is a possibility (weighted by a sticking coefficient $S_0 \in [0,1]$[14,43]) that it bounces and continues its journey with another trajectory until it reaches a new site or until it reaches the roof of the simulation domain. In that case, the particle disappears and another particle with a different trajectory is generated. In this simplified scheme (only first neighbors are considered), the new trajectory is obtained assuming specular reflection of the bouncing particle. At this point, it is evident that the value of the sticking coefficient in our model is not influenced by the angle of the trajectory of the arriving particle with respect to the surface.

iii) In addition to deposition, our model includes surface diffusion: once at the surface, the movement of a coarse particle is simulated by jumping from lattice site to lattice site—as explained before—via a random walk mechanism, characterized by a jump rate,

$$\Gamma_l = \frac{6D_0}{a_0^2} e^{-(\Delta E_l/K_B T)}, \quad (4)$$

where the subindex of Γ_l labels a particular diffusion event from a list $(l = 1, ..., L)$, T is the substrate temperature, K_B is the Boltzmann constant and the pre-factor $6D_0/a_0^2$ define the time scale of the jump, D_0 being a parameter of the model is interpreted as a microscopically averaged diffusion coefficient. The activation energy, ΔE_l, for a diffusion event is calculated as,

$$\Delta E_l = nE_b + mE_w + \delta E = \Delta E_l^0 + \delta E, \quad (5)$$

where E_b is the bond strength between particles of the film and E_w between the film and the substrate, n and m are the number of film and substrate neighbors, respectively—note that the index l comprises the terms n and m in a single label, $l \equiv (n, m)$—and δE is an extra energy term that accounts for the structural features associated with the simulated material. This is the approximation used in Elsholz et al.,[15,17,19,22] where the term δE accounts for the energy fluctuations associated with the local structural fluctuations in amorphous lattices.

In its basic form (i.e., without the term δE in the activation energy), the system has a very simple rate structure that depends on all possible $n + m$ combinations. However, here we assume that particles with five and six neighbors are immobile (max $(n + m) < 5$). With this constraint, the size of the list of diffusion rates is set at $L = 14$. Below we will describe the calculation details of this term, which are very different depending on if we are treating the amorphous or the anisotropic case.

The simulation begins with an initially bare flat substrate on which we grow the film following the BKL scheme. In this scheme, one must generate lists with the total rates of all the individual processes that take place in the simulation: the deposition rate, the total diffusion rate of all particles with rate $\Gamma_{l=1}$, with rates $\Gamma_{l=2}$ and so on. This algorithm ensures that "something happens" always on each cycle, no matter what. In each cycle of the algorithm, any of the possible events of the model (deposition or diffusion) can be chosen according to its probability of occurrence. Once an event is executed, the physical time of the simulation is updated with a time interval that depends on the total rate of the system on each cycle. If a deposition event is chosen during a cycle of the simulation, a particle is launched toward the surface following the procedure described above. On the other hand, the particles already deposited can move across the surface via surface diffusion. Once the particle reaches the surface, a δE value is assigned to it based on the type of material and the particle neighborhood.

Note that, due to its size, each simulated mesoscopic particle may contain hundreds of atoms. So we would be talking about "clusters" of atoms that jump on the surface as a whole. In this sense, the time that must elapse for one of these clusters to move completely will be greater

than the time that a real atom takes to jump. This means that by increasing the size of the particle we are necessarily decreasing the time resolution of the simulation. The parameters associated with jump rates should reflect this fact.

Finally, it is important to recognize that effects like sublimation or knock-in effects, related to the kinetic energy of the arriving particles, are assumed as residual under the experimental conditions considered here and therefore are ignored in the model. First, in our experiments, we do not work at the low pressures expected in a typical ECR growth (i.e., ~10^{-5}–10^{-3} mbar).[44] In addition, we also have a stainless-steel grid with 3 mm diameter round holes and a transparency of 50% separating the plasma glow from the sample holder within the growth chamber, which reduces the arrival of ions.[45]

3.1 | Amorphous material

For the case of amorphous materials, δE can randomly fluctuate spatially within an interval defined by the parameter Δ ($\delta E \in [0, \Delta]$). In our model, we apply a regular discretization to this energy interval, forming an array with N_a elements evenly distributed, $\delta E = (\delta E_1, \delta E_2, ..., \delta E_\mu, ..., \delta E_{N_a})$, where $\delta E_1 = 0$ and $\delta E_{N_a} = \Delta$. The index associated with this discretization helps us to add an identification label to the particle. In this way, a particle located at the site (i, j, k) and having an associated value δE_μ ($\mu = 1, ..., N_a$) is labeled as $G_{i,j,k} = \mu + 1$. If the arriving particle is on the bare substrate and has no film neighbors (only substrate), the index μ is set randomly from a uniform distribution. On the contrary, if one or more film neighbors are present δE_μ is obtained by averaging the corresponding δE values of those neighbors. For diffusion events one follows a similar criterion: once the particle jumps to another position, the neighborhood of the arrival site is scanned to set the new δE_μ. Note that this procedure introduces implicit lateral spatial correlations among the particles. The search radius for the averaging procedure may be changed to control the degree of correlation.

3.2 | Anisotropic material (wurtzite)

As in the amorphous case, we simulate the surface diffusion in wurtzite-type materials like ZnO by means of an extra term δE in the activation energy. However, in this case, δE is defined as a function of the local morphology and crystallographic orientation. For this purpose, we define two coordinate systems: a local one centered on the particle and whose coordinates are

labeled as $x' = [11\bar{2}0]$, $y' = [10\bar{1}0]$, $z' = [0001]$, and a global coordinate system whose axes x, y, and z coincide with those of the three-dimensional grid (the z-axis is set normal to the flat substrate). Any rotation of the coordinates system of the particle (x',y',z') with respect to the global coordinates system (x,y,z), is parameterized by a set of Euler's angles (θ, φ, γ) (see Figure 3a,b). Again, a particle deposited on the bare substrate, with no film neighbors, is initially labeled with one crystal orientation chosen at random following distribution that can be uniform or weighted. If there are one or more film neighbors, we scan them and assign to the particle the crystallographic orientation of the majority of neighbors. In that situations where we have a tie between two or more options (e.g., if we have only two neighbors each with different Euler parameters), we randomly choose one of these. A similar criterion is applied at the arrival site after a surface diffusion event.

The process of assigning the crystallographic orientation to a coarse particle deposited on the bare substrate begins by applying a regular discretization to the angles (θ, φ, γ): $\theta = (\theta_1, ..., \theta_s, ..., \theta_{N_\theta})$, $\varphi = (\varphi_1, ..., \varphi_p, ..., \varphi_{N_\varphi})$ and $\gamma = (\gamma_1, ..., \gamma_q, ..., \gamma_{N_\gamma})$. Thus, one gets a set of three numbers (s, p, q), which characterize a particular orientation of the crystal axes. This set is comprised of a single label, μ, which helps us to identify the particle by its associated crystallographic orientation with respect to the substrate ($G_{i,j,k} = \mu + 1$).

As mentioned above, the calculation of δE requires considering the local landscape around the particle that we want to move. As in the amorphous case, δE_μ is defined within the interval $[0, \Delta]$. In this case, however, we do not apply a regular discretization to the interval since the discretization is applied to the Euler's angles. Instead, here the value of δE_μ of a particle is defined as the extra energy added to its diffusion barrier by a set of far-located grid points (up to a maximum of eight, in which case $\delta E_\mu = \Delta$) surrounding the particle and distributed in an approximate hexagonal bipyramid shape, as is shown in Figure 3c. The spatial distribution of these points (referred from now as *mesoscopic neighbors*) is chosen to ensure the hexagonal symmetry of these mesoscopic bonds, which will serve to reproduce the crystal-related features of the growing film (e.g., different growth velocities for different crystal orientations). As can be seen in Figure 3c, two of the eight mesoscopic neighbors are aligned parallel to the local c-axis of the wurtzite [0001], and the remaining six form an (approximate) hexagonal arrangement in the c-plane. We assume that the contribution of these *mesoscopic bonds* along the c-axis ($\delta E_\parallel$) may be different from that of the c-plane ($\delta E_\perp$). This difference is quantified using an *anisotropy ratio* A_r ($\delta E_\parallel = A_r \delta E_\perp$):
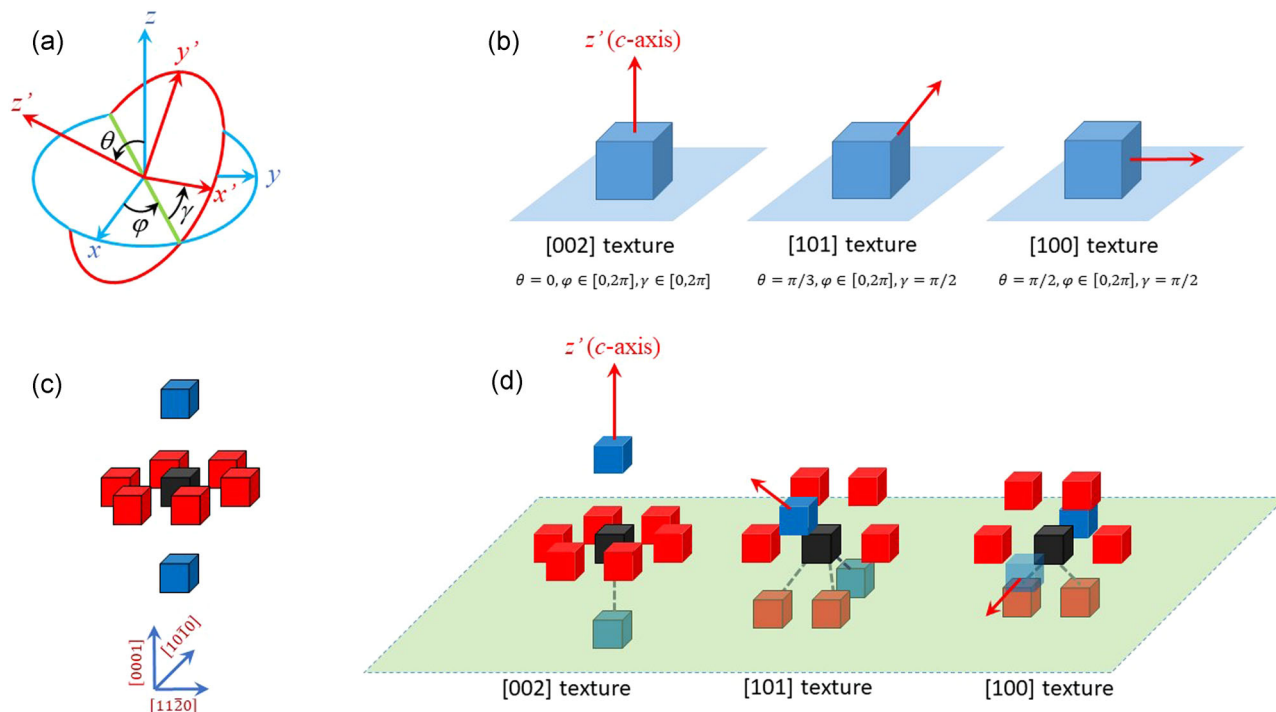
FIGURE 3 (a) The set of Euler's angles used in this study to describe the rotations of the local crystallographic system (x', y', z'), centered in the particle, with respect to the global system (x, y, z) linked to the substrate (where z is set normal to the substrate surface). (b) Three examples of a single ZnO particle attached to the bare substrate surface having the three crystal orientations considered in this study. (c) The 3D arrangement of long-range (mesoscopic) neighbors is considered in the calculation of δE_μ. The arrangement has the shape of a hexagonal bipyramid with the hexagonal plane normal to the c-axis of the central particle (black cube). Each bond with the blue particles has strength $\delta E_\parallel = A_r \delta E_\perp$, whereas each one of the six bonds with the red particles has strength $\delta E_\perp$. (d) Three examples of the criteria followed to counting the mesoscopic bonds during the calculation of δE_μ: for a single particle (black cube) attached to a flat surface parallel to the substrate, the number of mesoscopic bonds depends on the orientation of the particle's crystal axes. The bonds taken into account on each case (those which are beneath the surface) are highlighted by thick dashed lines

$$\Delta = 2\delta E_\parallel + 6\delta E_\perp = 2(A_r + 3)\delta E_\perp, \quad (6)$$

where the subscripts ∥ and ⊥ must not be confused with the label μ. The set of angles associated with label μ permits us to identify the location of the eight sites that must be checked to get δE_μ. Starting from the unit vector $\hat{n} = (\cos\varphi \sin\theta, \sin\varphi \sin\theta, \cos\theta) = (n_x, n_y, n_z)$, the positions of the two mesoscopic neighbors (labeled $+$ or $-$) located along the c-axis of the particle are obtained from $i_\pm = i \pm N_r \text{Int}(\sqrt{1 + N_r}\, n_x)$, $j_\pm = j \pm N_r \text{Int}(\sqrt{1 + N_r}\, n_y)$ and $k_\pm = k \pm N_r \text{Int}(\sqrt{1 + N_r}\, n_z)$, being (i,j,k) the position of the central particle and N_r an integer parameter that enables us to tailor the overall distance between these neighbors and the central particle (below we justify this point. In all the ZnO growth simulations shown in this study we have set $N_r = 2$). Now, to find the position of the m-neighbor from the remaining six in the c-plane, we define first a unit vector $\hat{e}_0 = (\cos\gamma', \sin\gamma', 0)$, with $\gamma' = \gamma + (m - 1)\pi/3$. Next, we apply two rotations to this vector, $\hat{e} = (e_x, e_y, e_z) = R_z(\varphi)\ R_y(\theta)\ \hat{e}_0$, where:

$$R_y(\theta) = \begin{pmatrix} \cos\theta & 0 & \sin\theta \\ 0 & 1 & 0 \\ -\sin\theta & 0 & \cos\theta \end{pmatrix} \text{and} \quad (7a)$$

$$R_z(\varphi) = \begin{pmatrix} \cos\varphi & -\sin\varphi & 0 \\ \sin\varphi & \cos\varphi & 0 \\ 0 & 0 & 1 \end{pmatrix} \quad (7b)$$

Finally, the position of the m-neighbor is calculated following: $i_m = i + N_r \text{Int}(\sqrt{1 + N_r}\ e_x)$, $j_m = j + N_r \text{Int}(\sqrt{1 + N_r}\ e_y)$, and $k_m = k + N_r \text{Int}(\sqrt{1 + N_r}\ e_z)$. Obviously, empty sites $(G_{i,j,k} = 0)$ are not considered in the calculation (see Figure 3d), so we will always have to count less than eight mesoscopic bonds:

$$\delta E_\mu = n_\parallel \delta E_\parallel + n_\perp \delta E_\perp\ (n_\parallel \le 2 \quad \text{and} \quad n_\perp \le 6). \quad (8)$$

It is important to mention that the mesoscopic neighbors are in positions beyond the layers of first and second neighbors (in fact, this separation may be tuned

to even larger values by means of parameter N_r). The reason for this is the angular resolution needed to reproduce approximately the hexagonal shape of the c-plane neighbor arrangement and to provide a minimum resolution to reproduce the different crystal orientations during the simulation. This is one of the main limitations of the use of a cubic grid for our KMC simulator. Finally, the interaction between particles belonging to different textured domains (grain boundaries) is addressed as follows: we assume that the strength of each mesoscopic bond during the evaluation of δE_μ is reduced by a factor that depends on the difference between the crystal orientation of the central μ-particle with that of each of those mesoscopic neighbors. Thus, the Equation (8) is restated as:

$$\delta E_\mu = \sum_{\rho=1}^{2} \delta E_\| M_{\mu,\rho} + \sum_{\sigma=1}^{6} \delta E_\perp M_{\mu,\sigma}, \qquad (8')$$

with $M_{\mu,\upsilon} = \cos^2(\Delta\theta_{\mu,\upsilon})\cos^2(\Delta\varphi_{\mu,\upsilon})\cos^2(\Delta\gamma_{\mu,\upsilon})$, in which $\Delta\theta_{\mu,\upsilon}$, $\Delta\varphi_{\mu,\upsilon}$, and $\Delta\gamma_{\mu,\upsilon}$ represent the difference between the Euler's angles of the crystal orientation of particles μ and υ. During the simulation, the selection of a particular event is performed through the standard BKL scheme excluding the term δE_μ. This is done to avoid increasing the size and complexity of the events list of the algorithm. Once an l-event with rate Γ_l is selected, the term δE_μ is included by means of an acceptance-rejection method.[46] The procedure is the following: since $\delta E_\mu > 0$, by summing this term to the activation energy δE_l^0 one gets a new rate, $\tilde{\Gamma}_l$, that its lower than the original ($\tilde{\Gamma}_l \leq \Gamma_l$). In that sense, the rate Γ_l represents the upper limit in an interval of possible values per each L-type event. Once we get $\tilde{\Gamma}_l$, a uniformly distributed random number $\zeta_1 \in [0,1)$ is generated and compared with the ratio $\tilde{\Gamma}_l/\Gamma_l$. If $\zeta_1 < \tilde{\Gamma}_l/\Gamma_l$ the jump is performed. On the contrary, another particle is selected for jumping following the same procedure. The computation time wasted in this acceptance-rejection procedure will depend on how small is the ratio $\tilde{\Gamma}_l/\Gamma_l$.

Once a particle is selected for jumping, the jump direction is chosen by searching the available neighbor sites. In general, the arrival site is selected randomly except when a step is encountered. In that case, the probability of the jump to that site is reduced by a factor $e^{-(\zeta_2/K_B T)}$, ζ_2 being a uniform random number ($\zeta_2 \in [0, E_s]$, where E_s is an energy parameter of the model). Note that, although Schwoebel-like barriers are found to be negligible in amorphous materials,[47] we consider it necessary to include a step-barrier here to hind the intrinsic cubic nature of our CG computational array under a wider range of growth conditions, where diffusion processes play a major role. Nevertheless, the inclusion of randomness for this barrier permits us to approach the lack of slope selection characteristic of amorphous film morphologies. Finally, to visualize the simulations, the coordinates of all the particles are saved in xyz format. Thus, the files were loaded in *Ovito*,[48] a 3D visualization software suitable for this purpose.

4 | RESULTS AND DISCUSSION

4.1 | Nanoporosity and scaling behavior of (amorphous) TiO_2 thin films

In the case of TiO_2, in all the simulations we have considered an array of $201 \times 201 \times 1001$ with a grid step of $a_0 = 2.5$ nm, which gives us a surface area of size 500×500 nm^2. The nominal growth rate (nominal thickness vs. time) has been set at 4 nm/min (0.027 ML/s). The rest of the parameters of the model have been set to $D_0 = 3 \times 10^3$ nm^2/s, $E_b = 0.08$ eV, $E_w = E_b$, $E_s = E_b/2$, and $\Delta = E_b/2$ (for the discretization of the fluctuating energy term we set $N_a = 41$). These parameters are grouped in Table 1. Finally, all the simulations are carried at RT.

Figure 4a,b gather the characteristic SEM cross-section and top view micrographs of a TiO_2 thin film fabricated by PECVD under the experimental conditions detailed in the Section 2; RMS values as a function of the thin film thickness are represented in Figure 4c. In addition, Figure 5a–d shows the evolution of the morphology of the film as a function of the amount of material deposited (coverage), considering two different angular distributions for the flux of arriving particles. In both cases, we have set the value of the sticking coefficient S_0 at 1 and 0.65.[14] We can verify that, in all cases, the morphologies depict a columnar-like formation, which is in good agreement with the SEM micrographs, as shown in Figure 4. On the other hand, when the flow of arriving particles is more dispersed ($\upsilon_n = 0$), the separation between these columns tends to be larger. Also, although in both cases the diameter of the columns tends to increase with the thickness of the film, in Figure 4a this increase is much more evident. This last result is known to be a consequence of the shadowing effect and is directly related to the angular dispersion of the particle flow.[16,22,49]

In general, several of the morphological characteristics observed can be quantified in terms of the RMS roughness:

$$w(t) = \sqrt{\langle (h(r_\perp, t) - \bar{h}(r_\perp, t))^2 \rangle_{r_\perp}}, \qquad (9)$$

where $\langle ... \rangle_{r_\perp}$ denote average with respect to in-plane coordinates $r_\perp$, $h(r_\perp, t)$ is the local height at $r_\perp$ and $\bar{h}(r_\perp, t) = \langle h(r_\perp, t) \rangle_{r_\perp}$. Starting from $w(t)$, the dynamic

TABLE 1 Parameters used in the growth simulations of amorphous TiO_2 thin films

|			
Size of the 3D grid ($N_x \times N_y$)	$201 \times 201 \times 1001$	Grid step size a_0 (nm)	2.5
Growth rate (nm/min)$\times N_z$	4	Coverage (nm)	1000
D_0 (nm^2/s)	3000	Temperature (K)	300
E_b (eV)	0.08	E_w (eV)	0.08
E_s (eV)	0.04	Δ (eV)	0.04
N_a	41		
Sticking coefficient S_0	(0.65, 1)		
Normalized velocity v_0	(0, 0.73)		

properties of the film can be described according to a power law, $w(t) \sim t^\beta$ (or $w(h_0) \sim h_0^\beta$, h_0 being the coverage), characterized by an effective growth exponent β. The different growth regimes are quantified in this way in terms of the value of β.[15,17,49] Values of $\beta > 0.5$ obtained experimentally for the case of TiO_2, SiO_2, and organic films are attributable to the amorphous character of the material, although later it has been observed that the angular distribution of trajectories of the arriving atoms also plays a very important role via the shadowing effect[16,22,49] (see Figure 4c). This can be observed in Figure 5c, where the effective growth exponents differ significantly from each other. In the case of the isotropic angular distribution ($v_n = 0.73$) it is even observed that the values obtained are around 0.5 for the growth conditions (growth rate and temperature) considered here.

Under these conditions, when we consider a sticking coefficient equal to 0.65, we obtain a value of β similar to that obtained in Figure 4c. Note that the increase in angular dispersion ($v_n = 0$) translates into a larger response of the morphology to changes in S_0. For instance, when $v_n = 0$ the difference between the RMS roughness at maximum thickness of cases $S_0 = 0.65$ and $S_0 = 1$ is approximately three times (~ 35 nm) the difference when $v_n = 0.73$ (~ 10 nm). However, the situation with the effective growth exponent is different. In this case, larger β values show smaller S_0-dependent changes for $v_n = 0$ than for $v_n = 0.73$. The foregoing shows that the proportionality constant in $w(h_0)$ is strongly dependent on the shadowing and plays an important role when one faces deposition flows with wide angular dispersion. Thus, when shadowing tends to be dominant with respect to diffusion events, the morphology of the film tends to be more sensitive to small changes in the material-related properties. As was found in Borrás et al.,[22,49] no surface diffusion of TiO_2 *ad-species* is expected under the Full O_2 plasma growth conditions of Figure 4a–c, so a high sticking coefficient and a low surface diffusivity yield the observed columnar growth when these conditions are combined with isotropic angular dispersion of the flow of incoming particles, typical of the PECVD technique. This conclusion is complemented by our results, which show that for an angular dispersion shifted toward more horizontal trajectories, the shadowing effect is boosted, and the columns grow faster, with a wider dispersion of heights and with more space between them.

4.2 | Microstructure and texture properties of polycrystalline ZnO thin films

For the case of wurtzite-type ZnO, we have considered a grid with $201 \times 201 \times 1001$ elements, a grid step of $a_0 = 1.625$ nm, and a surface of size 375×375 nm^2. The energy parameters have been set to $D_0 = 3 \times 10^2$ nm^2/s, $E_b = 0.09$ eV, $E_w = E_b$, $E_s = E_b/2$, and $\Delta = 3E_b$. The values of the v_n and S_0 parameters have been set to 0 and 1, respectively. The parameters used in this section are grouped in Table 2. Regarding the initial conditions, the code developed allows establishing a selection of permitted textures for the particles that arrive at the surface of the substrate. In this way, when a particle is deposited on the substrate, the crystallographic orientation that will be assigned to it will be chosen randomly within the selection of allowed textures. The objective of this control possibility is to be able to play with the possible influence of the substrate itself on the texture of the first clusters in the initial instants of growth. The origin of the texture shown by ZnO thin films under different growing conditions and the question as to whether this is defined early on or is progressively defined during the growth through a process of evolutionary competition of textured grains/domains is still under discussion. For this study, in the examples shown below we have considered it sufficient that the particles that arrive at the surface can be labeled with one of only three possible textures with equal probability: [002] ($\theta = 0$, $\varphi = \zeta_a 2\pi$, $\gamma = \zeta_b 2\pi$) [101] ($\theta = \pi/3$, $\varphi = \zeta_a 2\pi$, $\gamma = \pi/2$) and [100] ($\theta = \pi/2$,
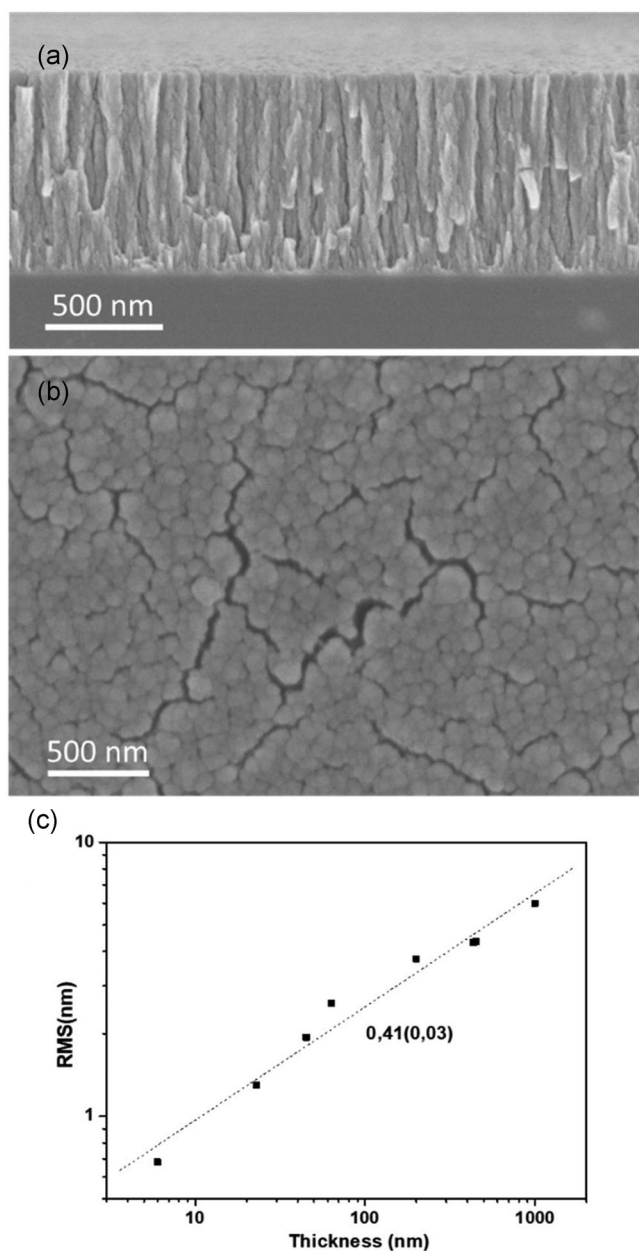
FIGURE 4 Scanning electron microscopic (SEM) cross-section (a) and top-view (b) micrographs showing the columnar-like morphology of the TiO_2 plasma-enhanced chemical vapor deposition thin films deposited at room temperature. (c) Experimental estimation of the β parameter from the root mean square (RMS) values obtained by atomic force microscopy characterization of films with increased thickness

$\varphi = \zeta_a 2\pi, \gamma = \pi/2$), being $\zeta_{a,b}$ two uniformly distributed random numbers within the interval [0,1]. Finally, to study texture-related characteristics of the simulated films and to be able to make better comparisons with experiments, we calculate the texture coefficients in our samples. To obtain the texture coefficient for a particular crystal orientation, for example [002], we sum up all those particles labeled with that texture and divide the

result by the total number of particles of the film (i.e., excluding the particles of the substrate). These values have been compared with the experimental texturing coefficients obtained from the XRD patterns (see Section 2).

Figure 6 shows top-view and cross-section images of a ZnO film fabricated on substrates at RT conditions under oxygen plasma and growth rate of 10 nm/min (Figure 6a,b), the corresponding XRD pattern acquired under Bragg–Brentano configuration normalized to the higher peak for different thicknesses (Figure 6c) and the calculated texturing coefficients (Figure 6d). Figure S1 in the Supporting Information Section gathers the XRD patterns for ZnO thin films deposited under different conditions of substrate temperature, growth rate, and thickness.

Figure 7 shows the morphology obtained for different ZnO films considering several values of the anisotropy ratio, A_r. In these simulations, the temperature of the sample has been set at RT and the nominal growth rate at 5 nm/min (Figure 7a,b) and 10 nm/min (Figure 7c,d), which correspond to growth rates of approximately 10 and 20 nm/min, respectively, if we calculate them in terms of the film thickness (as in the experiments) rather than the nominal coverage. In Figure 7a,c, the morphology of each film is highlighted, while in Figure 7c,d the chosen colors make it possible to highlight the textures of the different domains (grains) that appear in each case. The first feature that can be verified is the values of A_r that are much larger than 1—which means a higher growth rate along the c-axis of the wurtzite than in a direction perpendicular to it—give rise to a film that is almost totally [002]-textured. The columnar morphology associated with this texture is reasonably consistent with the results in Figure 6 and previous results for thin films fabricated under similar growth conditions[33] (see also Figure S1). Due to shadowing effects, the observed columns are narrow at the base and tend to increase in diameter with increasing thickness. As we reduce the value of A_r for a growth rate of 5 nm/min (real growth rate ~10 nm/min), an increasingly abundant presence of [101]-textured domains is observed. The consequences in morphology are quite evident: the nano-columns tend to show a slightly tilted axis and their cross-section turns out to be anisotropic, showing a rather pronounced elongation perpendicular to the [002] axis. As we approach toward, that is, when the growth rates parallel and perpendicular to the c-axis are equal, the texture of the film changes again rapidly and becomes mostly [100]. In this region, the nanocolumns continue to show an evident anisotropy in their cross-section. On the other hand, these recover the verticality previously observed when the texture was [002]. The elongated cross-sectional shape of the nanocolumns for $A_r \leq 1.5$ agrees very well with the morphology shown in Figure 6a. Likewise, their slight tilt, as observed in Figure 6b, coincides
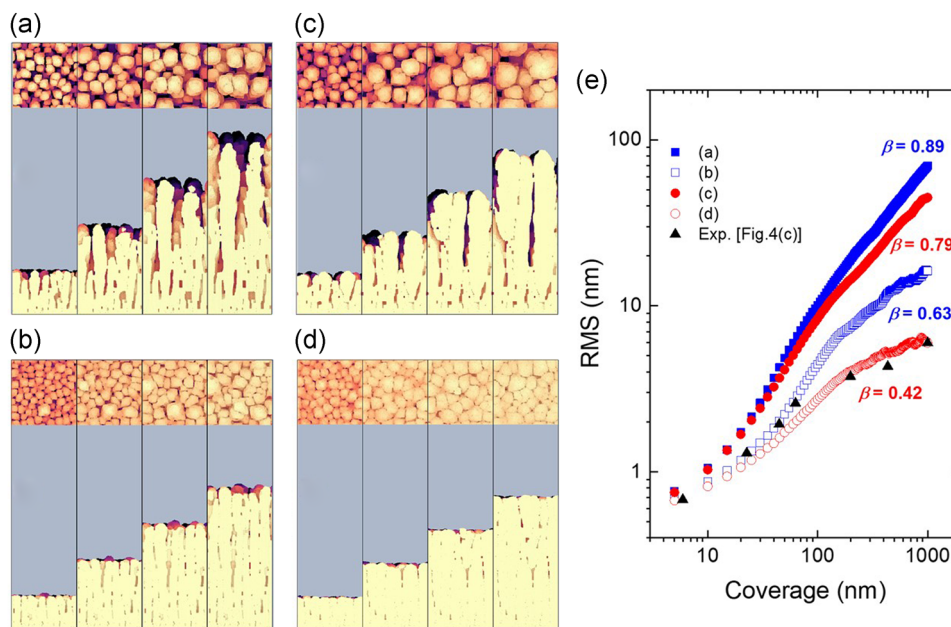
FIGURE 5 Simulated film morphologies at coverages 250, 500, 750, and 1000 nm for (a) $v_n = 0$; $S_0 = 1$, (b) $v_n = 0.73$; $S_0 = 1$, (c) $v_n = 0$; $S_0 = 0.65$ and (d) $v_n = 0.73$; $S_0 = 0.65$. Evolution of the calculated root mean square (RMS) roughness as a function of thickness for cases (a–d). The black triangles are the experimental data of Figure 4c. The growth exponents obtained for each case are shown. The rest of the simulation parameters are described in the text

TABLE 2 Parameters used in the growth simulations of polycrystalline ZnO thin films

Size of the 3D grid ($N_x \times N_y \times N_z$)	$201 \times 201 \times 1001$	Grid step size a_0 (nm)	1.625
Growth rate (nm/min)	(5, 10)	Coverage (nm)	1000
D_0 (nm²/s)	300	Temperature (K)	300
E_b (eV)	0.09	E_w (eV)	0.09
E_s (eV)	0.045	Δ (eV)	0.27
$N_{\theta,\varphi,\gamma}$	17	A_r	(0.5, 1.0, 1.25, 1.5, 2, 2.5, 3)
S_0	1	N_r	2
v_0	0		

with the presence of [101]-textured domains in the film (see Figure 6c,d). This result is consistent with what was observed in the simulations for values of A_r between 1 and 1.25. We also study the effects of increasing the growth rate up to 10 nm/min (real growth rate ~20 nm/min). With respect to the previous examples, the effects of a larger growth rate are evident not only in the morphologies but also in the textures of the film. Particularly around $A_r \sim 1.5$. This time the film shows a direct transition from mostly [100]-textured to mostly [002]-textured as we move from $A_r = 0.5$ to $A_r = 2.5$, without passing throughout any [101]-textured stage.

The previous results are summarized in Figure 8, where the texture composition of each film is plotted as a

function of the coverage. At the smallest (and largest) values of A_r, the texture coefficients seem to be insensitive to changes in growth conditions. It is in the range $A_r = 1.0$–2.0 that the growth rate becomes relevant for the final texture of the films. In this region, it is possible to observe the competitive behavior of textured domains in some cases. Regarding this, a more detailed visualization of the growth process of the first deposited ~160 nm of ZnO, for values $A_r = 0.5$ and $A_r = 1.0$ at a growth rate of 5 nm/min, can be found in the Supporting Information (Figure S2). These correspond to the initial stages of the curves in Figure 8a,b.

Qualitatively, the behavior of the components [101,100] of the texture coefficients obtained in our
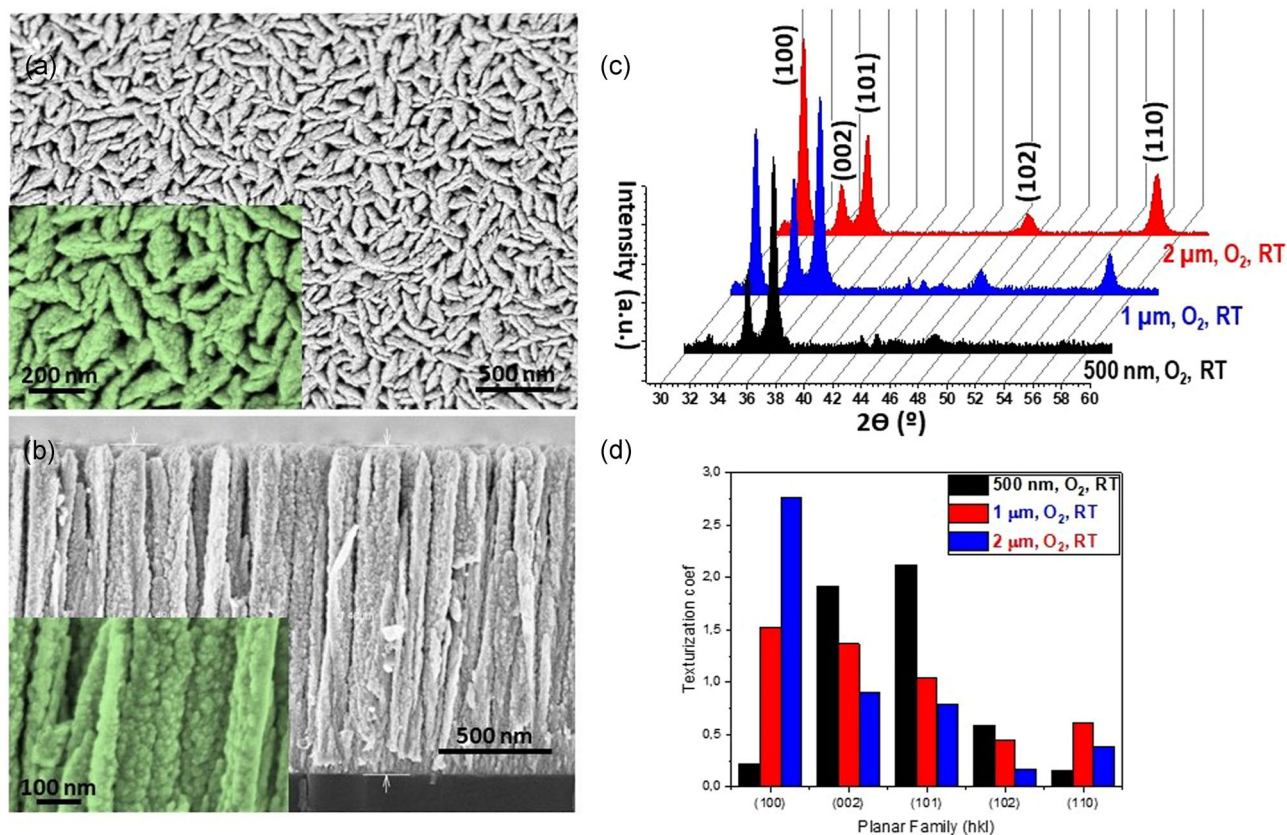
FIGURE 6 Scanning electron microscopic top-view (a) and cross-section (b) micrographs showing the columnar-like morphology of the ZnO plasma-enhanced chemical vapor deposition thin films deposited at room temperature (RT) under oxygen plasma for different thicknesses as labeled. (c) X-ray diffraction patterns acquired under Bragg–Brentano configuration (indication on the main planes for ZnO wurtzite) (d) and texturization coefficient for the samples deposited on fused silica substrates
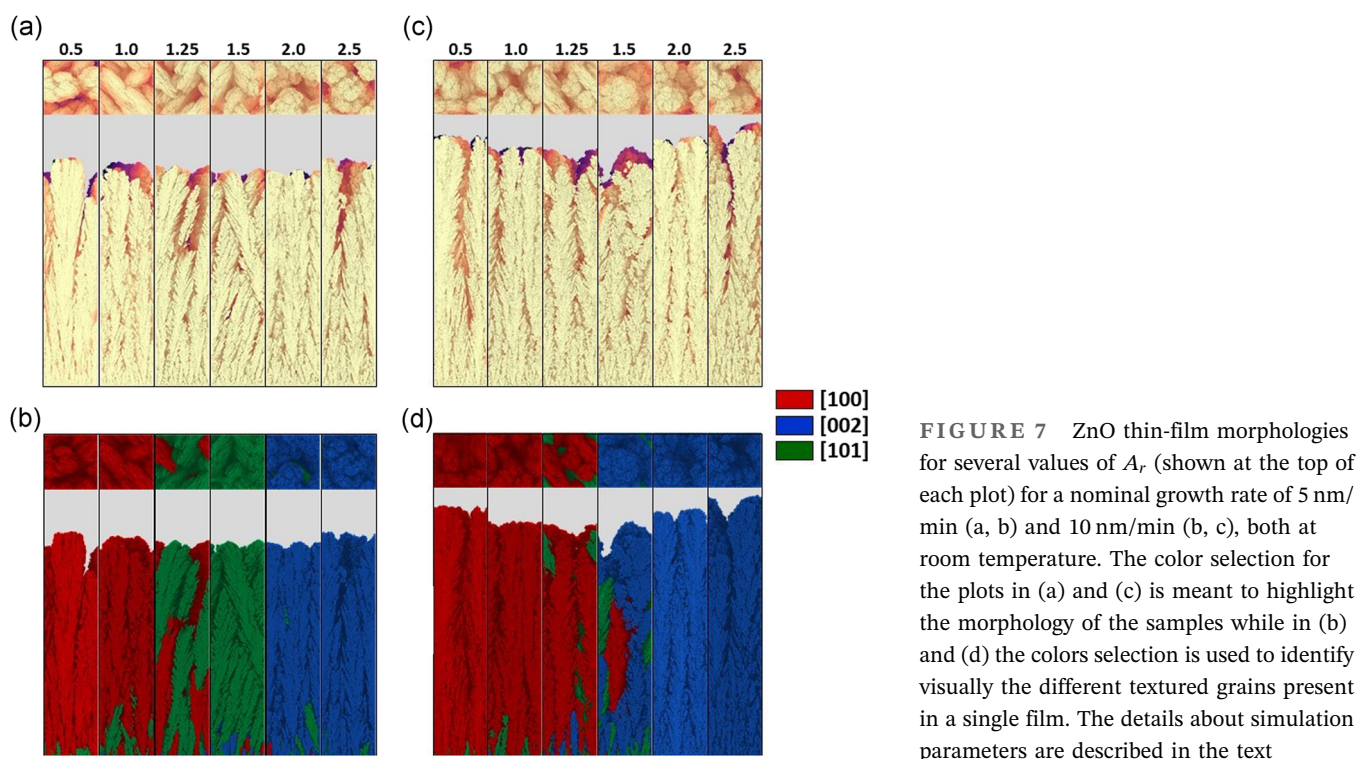

FIGURE 7 ZnO thin-film morphologies for several values of A_r (shown at the top of each plot) for a nominal growth rate of 5 nm/min (a, b) and 10 nm/min (b, c), both at room temperature. The color selection for the plots in (a) and (c) is meant to highlight the morphology of the samples while in (b) and (d) the colors selection is used to identify visually the different textured grains present in a single film. The details about simulation parameters are described in the text
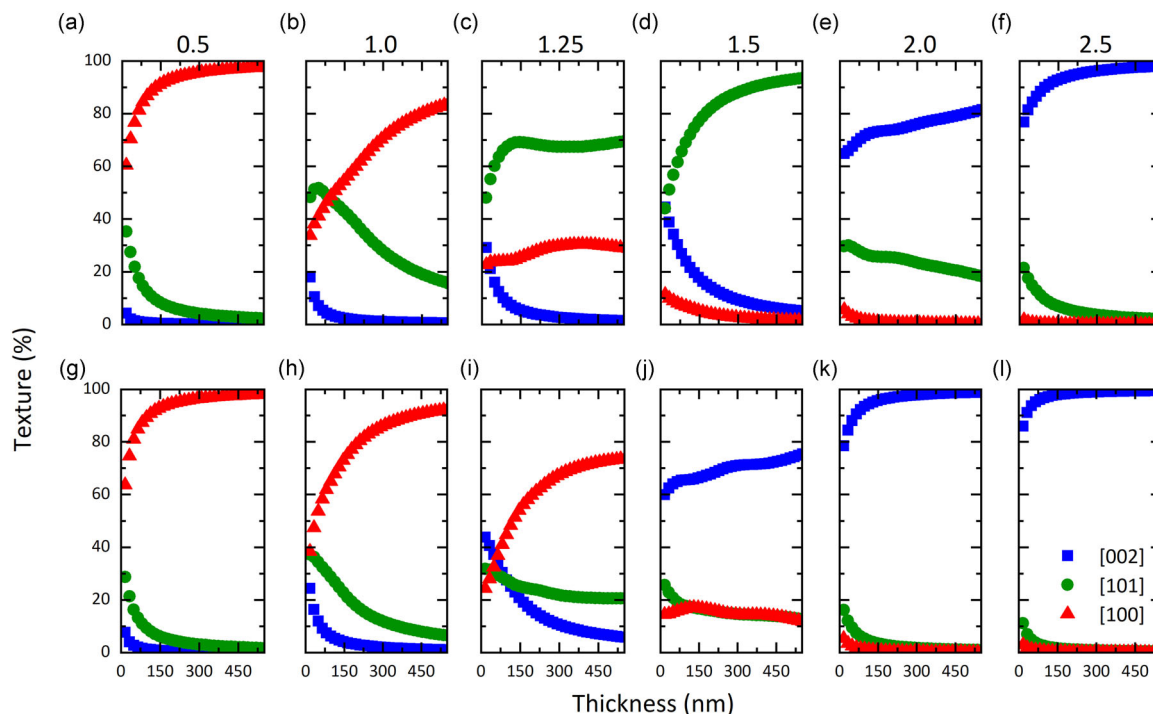
FIGURE 8 Evolution of the texture coefficients for the simulations shown in Figure 7 as a function of (nominal) coverage, evaluated for six values of A_r and considering the two different growth rates: (a–f) 5 nm/min and (g–l) 10 nm/min

simulations is similar to the results obtained in the real samples under similar growth conditions (Figure 6c,d). However, the evolution of the component [002] in the simulations is somewhat different from the experimental one. In our simulations, this component practically disappears at later stages of growth. This could be a consequence of the interaction with the substrate: just at the beginning of growth, the bare substrate surface would tend to favor the formation of nuclei or islands with texture [002] over textures [101] and [100]. Later, as growth advanced, evolutionary competition would favor the latter depending on the growth conditions ($A_r \leq 1.5$) but still with a noticeable presence of [002] domains. In principle, this may be addressed in our simulator by setting the arrival probability of [002]-textured particles higher than the other textures. This aspect will be addressed in greater detail in incoming work.

Finally, in Figure 9, the texture coefficient at maximum coverage for all the cases in Figure 8 is shown as a function of A_r. From this figure it is clear that when the values of the anisotropy ratio, A_r, lie within the range 1.0–2.0, the final texture of the film is more sensitive to changes in growth conditions, like the growth rate. Comparing our results with the amplitudes of the peaks in the XRD patterns of ZnO films shown in Vega-Poot et al.[50] (Figure 2), Figure 6, and Figure S1, we found a reasonable agreement with the relative values of our texture coefficients in Figure 9 for values of A_r between 1
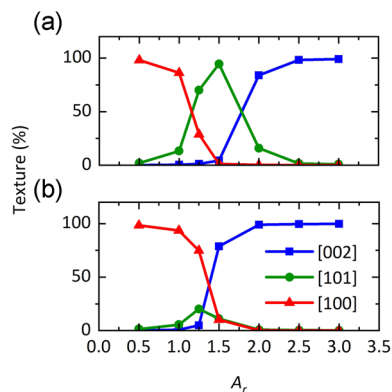
FIGURE 9 Texture coefficients at maximum thickness for the simulated ZnO thin films as a function of A_r (T = RT) for two different growth rates: (a) 5 nm/min and (b) 10 nm/min

and 1.5. In addition, our results at $A_r \geq 2$ agree well with the results shown in Romero-Gómez et al.[33] It is interesting to note that in the former case, the plasma composition was 90% O_2 and 10% H_2, whereas in the latter the sample is grown with pure oxygen plasma and for different power of the microwave source. This gives us a hint about the associated values of A_r on each case, suggesting that this parameter might be connected with specific microscopic surface features during the growth, which are related to the plasma composition.

The complex behavior that can be observed concerning the growth of textured domains would be explained in terms

of the interplay between the local crystallographic-orientation-dependent growth velocities and the flux of arriving particles. In connection with this, the bond strength along a particular direction can be associated with a higher local growth rate of the film in that direction. This idea is the main motivation behind this model. As an illustrative example, we can imagine a cluster or island of particles deposited on the substrate, all with their *c*-axis oriented perpendicular to the surface of the substrate (i.e., all particles with texture [002]). For example, a value of $A_r = 1.5$ means that the mesoscopic bonds along the *c*-axis are stronger than along any of the six bonds in the *c*-plane. Thus, as we let the system evolve with time, the island should tend to stretch its diameter and elongates along the *c*-axis. For $A_r < 1$ the opposite situation is found: the [002]-textured island should tend to increase its diameter while decreasing its height. A similar situation can be found if we include deposition in the process. In general, a particle that sticks in a surface having mesoscopic neighbors (below that surface) with the strongest bonds will tend to stay there more time before jumping. The overall number of mesoscopic neighbors taken into account in the calculation of δE_μ also plays a role in combination with their bond strength.

As deposition continues, particles that remain in the same site longer time have a higher probability of being buried by arriving particles. This process can be interpreted in terms of an increase in the velocity on which the material grows at that location. Obviously, once the first clusters are formed on the substrate surface just at the beginning of growth, each one with a particular texture, these will begin to grow in all directions with an angular distribution of velocities that will depend on the interplay between the anisotropy ratio and the number of mesoscopic bonds that each particle has on the surface of the clusters. As can be seen in Figure 3d a particle attached to a plain surface will have associated different numbers (and strengths) of mesoscopic bonds, depending on its crystallographic orientation. This difference is essential to understand the effect of the anisotropy ratio of this model on the competition between growing grains with different textures.

5 | CONCLUSION

In this study, we have developed a model based on the lattice KMC method to simulate the growth of thin films under conditions typical of vapor or vacuum deposition methods, such as PECVD. Using a CG approximation, the developed model allows the simulation of amorphous and anisotropic materials starting from a cubic three-dimensional array, which makes it particularly useful for reproducing

morphological characteristics at scales beyond the current possibilities of more sophisticated models, like MD or atomistic KMC, using moderate computational resources. The growth of TiO_2 at RT has been precisely simulated gaining insight into the mechanism behind the formation of columnar-shaped morphologies, giving a detailed view of the height dispersion and distance between columns. In the case of anisotropic crystalline materials, which represent the main novelty of this study, the model allows simulating the formation of grains with different textures within the same film (polycrystalline growth). We have chosen zinc oxide with a wurtzite structure as a proof-of-principle for this study. However, the approximation used for the hexagonal structure associated with wurtzite could be extended to other types of structures. At a qualitative level, we have found that the texture coefficients obtained for ZnO agree reasonably well with our experimental results and with some experimental results found in the literature, under growth conditions like those considered in this study.

It is important to recognize that ignoring the presence of [102] and [110] initial textures in our ZnO simulations might affect the dependence of textures on A_r. This is not only a parameter of the material but also of the growing conditions. In PECVD growth, the experimental conditions (plasma composition, etc.) can affect significantly the nature of surface processes of the growing film and can influence the preselection of allowed textures in the first instants of growth. Hence, the choice of allowed orientations should also be considered as a material-related parameter together with A_r. In that sense, many of the material properties that one would associate with A_r are also dependent on the experimental conditions. For the purposes of the current work, we have considered it sufficient to include the three main observed textures. However, the dependence of A_r on the relaxation of constraints for the initial texture selection has been left for a more detailed experimental study of the growth of ZnO under different growth conditions that is currently in process by our group and in which extensive use of the present simulator will be made.

CONFLICT OF INTERESTS

The authors declare that there are no conflict of interests.

DATA AVAILABILITY STATEMENT

The data that support the findings of this study are available from the corresponding author upon reasonable request.

ORCID

Jorge Budagosky http://orcid.org/0000-0003-0094-3490
Xabier García-Casas https://orcid.org/0000-0002-7165-3952
Juan R. Sánchez-Valencia https://orcid.org/0000-0003-2493-4433
Ángel Barranco https://orcid.org/0000-0002-8099-7669
Ana Borrás https://orcid.org/0000-0001-8799-2054

REFERENCES

[1] D. Chakraborty, G. N. Patey, *J. Phys. Chem. Lett.* **2013**, *4*, 573.
[2] M. Salvalaglio, C. Perego, F. Giberti, M. Mazzotti, M. Parrinello, *Proc. Natl. Acad. Sci. U. S. A.* **2015**, *112*, E6.
[3] U. Burghaus, *Surf. Rev. Lett.* **2001**, *8*, 353.
[4] T. Weckman, M. Shirazi, S. D. Elliott, K. Laasonen, *J. Phys. Chem. C* **2018**, *122*, 27044.
[5] S. Piana, J. D. Gale, *J. Cryst. Growth* **2006**, *294*, 46.
[6] S. Blackwell, R. Smith, S. D. Kenny, J. M. Walls, C. F. Sanz-Navarro, *J. Phys.: Condens. Matter* **2013**, *25*, 135002.
[7] A. L. Lloyd, R. Smith, S. D. Kenny, *J. Mater. Res.* **2018**, *33*, 847.
[8] R. Tonneau, P. Moskovkin, J. Muller, T. Melzig, E. Haye, S. Konstantinidis, A. Pflug, S. Lucas, *J. Phys. D: Appl. Phys.* **2021**, *54*, 155203.
[9] P. Smereka, X. Li, G. Russo, D. J. Srolovitz, *Acta Mater.* **2005**, *53*, 1191.
[10] S. S. Kelkar, C. A. Wolden, *J. Vac. Sci. Technol., B* **2014**, *32*(5), 052001.
[11] A. B. Aebersold, L. Fanni, A. Hessler-Wyser, S. Nicolay, C. Ballif, C. Hébert, D. T. L. Alexander, *Acta Mater.* **2019**, *173*, 74.
[12] A. A. Ramirez, I. Gil, G. Gordillo, A. M. Latifi, *Thin Solid Films* **2020**, *698*, 137846.
[13] R. W. Smith, *J. Appl. Phys.* **1996**, *81*, 1196.
[14] T. Karabacak, Y.-P. Zhao, G.-C. Wang, T.-M. Lu, *Phys. Rev. B* **2001**, *64*, 085323.
[15] F. Elsholz, E. Schöll, A. Rosenfeld, *Appl. Phys. Lett.* **2004**, *84*, 4167.
[16] A. Yanguas-Gil, J. Cotrino, A. Barranco, A. R. González-Elipe, *Phys. Rev. Lett.* **2006**, *96*, 236101.
[17] F. Elsholz, E. Schöll, A. Rosenfeld, *Phys. Stat. Sol. B* **2007**, *244*, 3639.
[18] T. O. Drews, R. D. Braatz, R. C. Alkire, *Int. J. Multiscale Comput. Eng.* **2004**, *2*, 313.
[19] R. Álvarez, A. Palmero, L. O. Prieto-López, F. Yubero, J. Cotrino, W. de la Cruz, H. Rudolph, F. H. P. M. Habraken, A. R. González-Elipe, *J. Appl.*Phys.* **2010**, *107*, 054311.
[20] R. Álvarez, P. Romero-Gomez, J. Gil-Rostra, J. Cotrino, F. Yubero, A. Palmero, A. R. González-Elipe, *J. Appl. Phys.* **2010**, *108*, 064316.
[21] F. Alvi, R. K. Joshi, Q. Huang, A. Kumar, *J. Nanopart. Res.* **2011**, *13*, 2451.
[22] A. Borrás, R. Alvarez, J. R. Sanchez-Valencia, J. Ferrer, A. R. Gonzalez-Elipe, *Microporous Mesoporous Mater.* **2012**, *160*, 1.
[23] T. Garnier, M. Nastar, *Phys. Rev. B* **2013**, *88*, 134207.
[24] P. Moskovkin, M. Panshenskov, S. Lucas, A. V. Solov'yov, *Phys. Stat. Sol. B* **2014**, *251*, 1456.
[25] N. M. Santhosh, G. Filipič, E. Tatarova, O. Baranov, H. Kondo, M. Sekine, M. Hori, K. Ostrikov, U. Cvelbar, *Micromachines* **2018**, *9*, 565.
[26] S. Mao, Z. Wen, S. Ci, X. Guo, K. Ostrikov, J. Chen, *Small* **2015**, *11*, 414.
[27] A. Mcleod, S. Kumar, K. C. Vernon, K. Ostrikov, *J. Nanomater.* **2015**, 230987.
[28] S. Ghosh, S. R. Polaki, M. Kamruddin, S. M. Jeong, K. Ostrikov, *J. Phys. D: Appl. Phys.* **2018**, *51*, 145303.
[29] A. N. Filippin, M. Macias-Montero, Z. Saghi, J. Idígoras, P. Burdet, J. R. Sánchez-Valencia, A. Barranco, P. A. Migdley, J. A. Anta, A. Borrás, *Sci. Rep.* **2017**, *7*, 9621.
[30] A. N. Filippin, J. R. Sánchez-Valencia, J. Idígoras, T. C. Rojas, A. Barranco, J. A. Antab, A. Borrás, *Nanoscale* **2017**, *9*, 8133.
[31] A. N. Filippin, J. R. Sánchez-Valencia, X. Garcia-Casas, V. Lopez-Flores, M. Macias-Montero, F. Frutos, A. Barranco, A. Borrás, *Nano Energy* **2019**, *58*, 476.
[32] N. Filippin, J. Castillo-Seoane, M. C. López-Santos, C. T. Rojas, K. Ostrikov, A. Barranco, J. R. Sánchez-Valencia, *ACS Appl. Mater. Interfaces* **2020**, *12*(45), 50721.
[33] P. Romero-Gómez, J. Toudert, J. R. Sánchez-Valencia, A. Borrás, A. Barranco, A. R. González-Elipe, *J. Phys. Chem.* **2010**, *114*, 20932.
[34] B. Boro, B. Gogoi, B. M. Rajbongshi, A. Ramchiary, *Renewable Sustainable Energy Rev.* **2018**, *81*, 2264.
[35] X. Hou, K. Aitola, P. D. Lund, *Energy Sci. Eng.* **2021**, *9*, 921.
[36] L. Lin, T. W. Jones, T. C.-J. Yang, N. W. Duffy, J. Li, L. Zhao, B. Chi, X. Wang, G. J. Wilson, *Adv. Funct. Mater.* **2021**, *31*, 2008300.
[37] R. K. Pandey, J. Dutta, S. Brahma, B. Rao, C.-P. Liu, *J. Phys. Mater* **2021**, *4*, 044011.
[38] X. Cao, Y. Xiong, J. Sun, X. Zhu, Q. Sun, Z. L. Wang, *Adv. Funct. Mater.* **2021**, *31*, 2102983.
[39] L. Yang, Z. Ma, Y. Tian, B. Meng, Z. Peng, *Micromachines* **2021**, *12*, 666.
[40] S. Korkmaz, I. A. Kariper, *Nano Energy* **2021**, *84*, 105888.
[41] A. B. Bortz, M. H. Kalos, J. L. Lebowitz, *J. Comp. Physiol.* **1975**, *17*(1), 10.
[42] W. J. Messe, T.-M. Lu, *J. Appl. Phys.* **2018**, *123*, 075302.
[43] T. Karabacak, *J. Nanophotonics* **2011**, *5*, 052501.
[44] A. Grill, *Cold Plasma in Materials Fabrication*, IEEE Press, Piscataway, NJ **1994**.
[45] D. Korzec, D. Theirich, F. Werner, K. Traub, J. Engemann, *Surf. Coat. Technol.* **1995**, *74–75*, 67.
[46] M. A. Saum, T. P. Schulze, C. Ratsch, *Commun. Comput. Phys.* **2009**, *6*, 553.
[47] H.-N. Yang, Y.-P. Zhao, G.-C. Wang, T.-M. Lu, *Phys. Rev. Lett.* **1996**, *76*, 3774.

**PLASMA PROCESSES
AND POLYMERS**

[48] A. Stukowski, *Modell. Simul. Mater. Sci. Eng.* **2010**, *18*, 015012.

[49] A. Borrás, A. Yanguas-Gil, A. Barranco, J. Cotrino, A. R. González-Elipe, *Phys. Rev. B* **2007**, *76*, 235303.

[50] A. G. Vega-Poot, M. Macías-Montero, J. Idígoras, A. Borrás, A. Barranco, A. R. González-Elipe, F. I. Lizama-Tzec, G. Oskam, J. A. Anta, *Chem. Phys. Chem.* **2014**, *15*, 1088.

SUPPORTING INFORMATION

Additional supporting information may be found in the online version of the article at the publisher's website.